Equivalent Circuit Derivation and Performance Analysis of a Single-Sided Linear Induction Motor Based on the Winding Function Theory

Wei Xu, *Member, IEEE*, Guangyong Sun, *Member, IEEE*, Guilin Wen, Zhengwei Wu, *Member, IEEE*, and Paul K. Chu, *Fellow, IEEE*

***Abstract*—A linear metro that is propelled by a single-sided linear induction motor (SLIM) has recently attracted much attention. Compared with the rotating-induction-machine drive system, the SLIM drive has advantages such as direct thrust without needing friction between the wheel and the railway track, small cross-sectional area, lack of gear box, and flexible line choice on account of the greater climbing capability and smaller turning circle. However, due to its cut-open primary magnetic circuit, the SLIM has a longitudinal end effect and half-filled slots on the primary ends, which can reduce the air-gap average flux linkage and thrust. Based on the winding function method, the SLIM is supposed to have the following three groups of windings: 1) primary windings; 2) secondary fundamental windings; and 3) secondary end effect windings. The proposed method considers the actual winding distribution and structure dimensions. It can calculate the mutual, self, and leakage inductance to describe the influence of the longitudinal end effect and half-filled slots. Moreover, a new equivalent model is presented to analyze the different dynamic and steady-state performance. Comprehensive comparisons between simulation and experimental results that were obtained from both one arc induction machine and one linear metro indicate that the proposed model can be applied to predict the SLIM performance and control scheme evaluation.**

***Index Terms*—Arc induction machine, dynamic-state performance, equivalent circuit model, half-filled slots, linear metro, longitudinal end effect, single-sided linear induction motor (SLIM), steady-state performance, winding function method.**

Manuscript received March 17, 2011; revised July 23, 2011, September 25, 2011, and November 23, 2011; accepted November 27, 2011. Date of publication January 11, 2012; date of current version May 9, 2012. This work was supported from in part by the National 973 Project of China under Grant 2010CB328005, the Key Laboratory for Automotive Transportation Safety Enhancement Technology, Ministry of Communication of the People's Republic of China, through the Open Fund under Grant CHD2011SY008, and the State Key Laboratory of Vehicle NVH and Safety Technology through the Open Fund under Grant NVHSKL-201002. The review of this paper was coordinated by Dr. W. Zhuang.

W. Xu is with the State Key Laboratory of Advanced Design and Manufacture for Vehicle Body, Hunan University, Changsha 410082, China, and also with the Platform Technologies Research Institute, RMIT University, Melbourne, VIC 3001, Australia (e-mail: weixuforhappy@gmail.com).

G. Sun (corresponding author) and G. Wen are with State Key Laboratory of Advanced Design and Manufacture for Vehicle Body, Hunan University, Changsha 410082, China (e-mail: sgy800@126.com; wenguilin@yahoo.com.cn).

Z. Wu and P. K. Chu are with the Department of Physics and Materials Science, City University of Hong Kong, Kowloon, Hong Kong (e-mail: wuzw@ustc.edu.cn; paul.chu@cityu.edu.hk).

Color versions of one or more of the figures in this paper are available online at http://ieeexplore.ieee.org.

Digital Object Identifier 10.1109/TVT.2012.2183626

NOMENCLATURE

α_1	Length of the entry-end-effect wave penetration coefficient (in meters).
α_2	Length of the exit-end-effect wave penetration coefficient (in meters).
σ	Secondary sheet conductivity $(1/(\Omega.\mathrm{m}))$.
η	Efficiency.
μ_0	Air permeability (in newtons per square ampere).
ω_e	Angular frequency of the power supply (in rad per second).
ω_r	Angular frequency of the rotor (in rad per second).
τ	Pole pitch (in meters).
τ_e	Half-wave length of the end-effect wave (in meters).
θ_s	Angle between the primary and secondary fundamental currents (in rad).
b_y	Flux density along the y-axis direction (in tesla).
g_e	Equivalent air-gap length (in meters).
$I_\mathrm{abc,s}$	Primary winding phase current in the ABC-axis (in amperes).
$i_{\alpha\beta,\mathrm{s}}$	Primary winding phase current in the $\alpha\beta$-axis (in amperes).
p_in	Input active power (in watts).
p_out	Output active power (in watts).
q_in	Input reactive power (in var).
s	Per-unit slip.
v_2	Motor operating speed (in meters per second).
F_e	Thrust (in newtons).
G	Goodness factor.
G_{sv}	Speed voltage coefficient matrix.
I_s	Primary phase current (in amperes).
I_re	Secondary-phase equivalent eddy current (in amperes).
J_1	Equivalent primary current sheet density (in amperes per meter square).
K_p	Winding pitch factor.
K_d	Winding distribution factor.
L_lr	Secondary leakage inductance (in henry).
L_ls	Primary leakage inductance (in henry).
L_m	Mutual inductance (in henry).
N_a	Number of primary series turns per phase.
$N_\mathrm{abc,s}$	Primary winding distribution functions in the ABC-axis.
$N_{\alpha\beta,\mathrm{s}}$	Primary winding distribution functions in the $\alpha\beta$-axis.

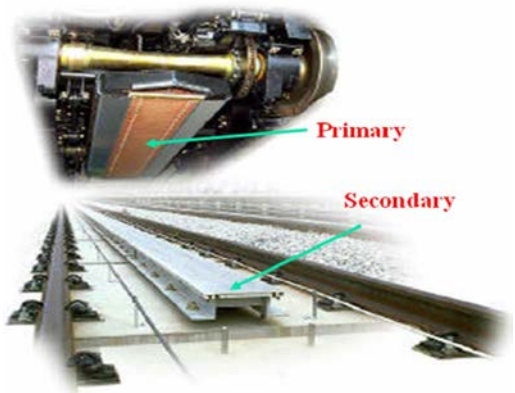

Fig. 1. Simple vehicle system diagram that is propelled by the SLIM.

$N_{\alpha\beta,\mathrm{rs}}$ Secondary fundamental winding distribution functions in the $\alpha\beta$-axis.
$N_{\alpha\beta,\mathrm{re}}$ Secondary end-effect winding distribution functions in the $\alpha\beta$-axis.
N_{se} Effective winding turns in series per phase.
R_{s} Primary resistance (in ohms).
R_{r} Secondary resistance (in ohms).

I. Introduction

CURRENTLY, more than 20 urban transportation lines that are propelled by single-sided linear induction motors (SLIMs) are commercialized worldwide, e.g., the linear metro in Japan, then Vancouver light train in Canada, and the Guangzhou subway line 4 [1], [2]. The typical SLIM drive system is shown in Fig. 1. It is shown that the SLIM hung below the redirector supplied by the inverter on the vehicle. The secondary is flattened on the railway track, and it usually consists of an aluminum sheet that is 5–10 mm thick and a 20-mm-thick back iron that acts as the return path for the magnetic flux [3]–[5]. Compared with rotary induction machine (RIM) drive systems, the SLIM system has the following merits. First, it can achieve direct propulsive thrust, independent of the friction between the wheels and rail, and can safely be operated, even in rainy or snowy weather [6]–[8]. Second, it has a smaller turning radius for its special bogie technique, smaller cross-sectional area for its omission of a gear box, larger acceleration, and stronger climbing ability due to its direct electromagnetic force. Hence, it offers a flexible line choice and reduced construction cost, which is particularly favorable for subway systems [9]–[11]. Third, it has lower noise and less maintenance without a gear box because of the nonadherent driving. Hence, it is an attractive mode of transportation in large cities [12].

However, as the SLIM primary moves, a new flux is continuously developed at the primary entrance side, whereas the air-gap flux quickly disappears on the exit side [13]–[15]. An eddy current in a direction counter to the primary current will be induced in the secondary sheet, and it correspondingly affects the air-gap flux profile along the longitudinal direction. This phenomenon is called the "longitudinal end effect." It can decrease air-gap average flux linkage (mutual inductance) and increase relevant copper loss as its speed goes up [16]–[18].

Due to extensive research, many papers are currently available with regard to the SLIM longitudinal end-effect analysis brought by the sudden generation and disappearance of the air-gap penetrating flux density. In [1] and [2], a single-phase T-model equivalent circuit is proposed to make electromagnetic design for SLIM and then study its steady performance. Based on the 1-D numerical analysis and relevant experimental verification, two coefficients are provided to describe the influence of the longitudinal end effect on the mutual and the secondary resistance. This method can be adopted in a wide-speed region and with different air-gap lengths. However, it is not suitable for studying the SLIM dynamic performance, such as the vector control or direct torque control algorithm, because it is only a steady-state equivalent circuit. In [4]–[6], one simple and useful function $f(Q)$ according to the hypothetical curve of the secondary eddy-current average value and the energy conversion balance theorem is presented. The function is affected by the SLIM speed, secondary resistance, secondary inductance, and some other structural parameters such as the primary length. For its simple equivalent model, it can easily be employed in different control algorithms similar to traditional induction machines. However, the function derivation is very coarse such that it is prone to increasing errors as the velocity goes up. In [7], steady- and dynamic-state performance by using the space harmonic method can theoretically be stimulated and the calculated results have comparatively high accuracy. However, this method requires substantially more computing time, and the accuracy mostly depends on many initially given parameters. If some key parameters are not rationally initialized, the final solution cannot be obtained due to nonconvergence. In [8], a Fourier series expansion was used to describe the influence of the end effects of SLIM. However, the time to attain higher accuracy in this technique can greatly increase for difficult determination of the mother wavelet. In [9], an equivalent pole-by-pole circuit model is derived from the viewpoint of primary winding distribution. It is suitable for the steady and transient performance analysis combined with different advanced control algorithms. Simulation results are verified by several experiments. Unfortunately, one set of tenth-order differential equations are needed to describe a basic model for a four-pole machine, and a higher order system of equations needs to be provided as the pole number goes up. Furthermore, some coefficients in this model mostly depend on experimental verification and are difficult to directly extend to other structures.

In this paper, through the winding function method, a new model is presented to study both the steady- and the dynamic-state performance of SLIM. Using the primary winding distribution, the longitudinal end effect and half-filled slots located in the primary ends are rationally taken into account in the winding function expressions.

II. Equivalent Circuits of the Single-Side Linear Induction Motor

According to Maxwell's law, the air-gap flux density equation of SLIM can be expressed by [17]

$$\frac{\partial^2 b_y}{\partial x^2} - \sigma\mu_0 v_2 \frac{\partial b_y}{\partial x} - j\sigma\mu_0\omega_e b_y = -j\mu_0 \frac{\pi}{\tau} J_1 e^{j(\omega_e t - \pi x/\tau)} \tag{1}$$

where σ is the secondary sheet conductivity, μ_0 is the air permeability, v_2 is the primary operating speed, $\omega_{\rm e}$ is the angular speed of the primary power supply, τ is the primary pole pitch, J_1 is the equivalent primary current sheet density, and $b_{\rm y}$ is the flux density along the y-axis direction. The solution of $b_{\rm y}(x,t)$ is

$$b_y(x,t) = \dot{B}_0\, e^{-j\frac{\pi x}{\tau}} + \dot{B}_1\, e^{-\frac{x}{\alpha_1}} e^{-j\frac{\pi x}{\tau_e}} + \dot{B}_2\, e^{\frac{x}{\alpha_2}} e^{j\frac{\pi x}{\tau_e}} \quad (2)$$

where $b_{\rm y}$ consists of the following three parts: 1) B_0; 2) B_1; and 3) B_2. B_0 is the normal traveling wave, which travels forward similar to the fundamental flux density in the RIM. B_1 and B_2, which are determined using boundary conditions, are the entrance- and exit-end-effect waves, respectively. α_1 is the penetration depth of the entry-end-effect wave, α_2 is the penetration depth of the exit-end-effect wave, and $\tau_{\rm e}$ is the half wavelength of the end-effect wave, which are functions of the speed and motor structural parameters [19], [20].

Based on the air-gap flux density equation, the SLIM secondary winding function is divided into the fundamental and end-effect components. First, it deduces the primary two-phase stationary axis model according to the primary actual winding distribution. Because there are no obvious windings on the secondary, the secondary winding function can be obtained from the field distribution theory [21]. In theory, the secondary winding function of the LIM consists of the following two independent components: 1) a fundamental part $N_{\rm rs}({\rm x})$ and 2) an end-effect part $N_{\rm re}({\rm x})$. It supposes that two electrically independent but mutually coupled secondary windings can be derived from the steady and dynamic states of the air-gap magnetic flux equations [22]. Moreover, it calculates all inductance, goodness factor, secondary resistance, and speed voltage coefficients. Based on the energy conversion relationship between the primary and the secondary [23], the mathematic expressions of thrust, power factor, and efficiency are derived. Generally, the whole derivation progress is quite complex, and more details can be found in [9] and [10]. A brief introduction on the theory of winding function is given as follows.

The winding function $N(x)$ of any winding is calculated by counting conductors. One example is the simple single-turn winding, as shown in Fig. 2(a). The conductors can be counted from left to right. If the current flows out of the paper, $N(x)$ is supported to increase by one, and when the current flows into the paper, $N(x)$ can decrease by one. Hence, it is easy to get the curve of $N(x)$ in Fig. 2(b). Although the winding function is a circuit concept, it can be related to field quantities. If Ampere's law is applied to Fig. 2(a) along the path A1A2 A3A4A1, then

$$\oint H \cdot dl = IN(x) \quad (3)$$

where H is the flux intensity, and I is the total winding current. If the iron is supported infinitely permeable, H is zero, except in the air gap along path A3A4. Hence, the air-gap flux intensity $H(x)$ can be described in terms of $N(x)$ as

$$H(x) = \frac{IN(x)}{g_e} \quad (4)$$

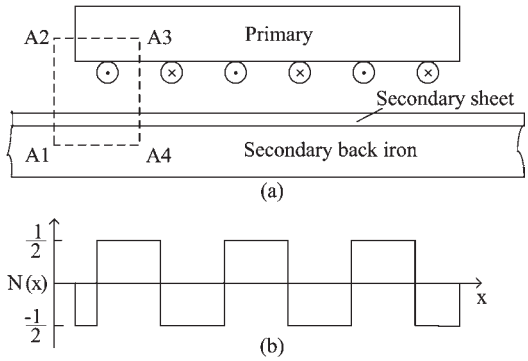

Fig. 2. SLIM with arbitrary winding distribution.

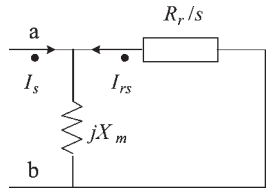

Fig. 3. One-dimensional model of the SLIM.

where $g_{\rm e}$ is the equivalent length of the air gap. Based on (4), the winding function $N(x)$ is equivalent to the magnetic motive force $IN(x)$ of the winding normalized by its current. Thus, it is independent of the machine excitation and relative to the machine geometry.

A brief summary of the expressions of three groups of winding functions is given as follows. The primary stationary three-axis winding functions are [9]

$$\begin{cases} N_{as}(x) = \frac{N_{se}}{2}\cos(\pi x/\tau + \pi) \\ N_{bs}(x) = \frac{N_{se}}{2}\cos(\pi x/\tau + \pi/3) \\ N_{cs}(x) = \frac{N_{se}}{2}\cos(\pi x/\tau - \pi/3) \end{cases} \quad (5)$$

where $N_{\rm se} = K_{\rm p}K_{\rm d}N_{\rm a}$, $K_{\rm p}$, and $K_{\rm d}$ are the winding pitch and distribution factors, respectively, and $N_{\rm a}$ is the number of primary series turns per phase. Hence, $N_{\rm se}$ is called the effective winding turns in series per phase.

To obtain the stationary two-axis stator winding function expressions $N_{\alpha{\rm s}}$ and $N_{\beta{\rm s}}$ from the stationary three-axis winding distributions, the following rules according to the theory of flux linkage balance should be obeyed by

$$N_{as}(x)i_{as}+N_{bs}(x)i_{bs}+N_{cs}(x)i_{cs}=N_{\alpha s}(x)i_{\alpha s}+N_{\beta s}(x)i_{\beta s} \quad (6)$$

where $i_{\alpha{\rm s}}$ and $i_{\beta{\rm s}}$ can be achieved from $i_{\rm as}$, $i_{\rm bs}$, and $i_{\rm cs}$ by using static 3/2 coordination transformation. Hence, the primary stationary two-axis winding functions are expressed by

$$\begin{cases} N_{\alpha s}(x) = \frac{3}{4}N_{se}\sin(\pi x/\tau) \\ N_{\beta s}(x) = -\frac{3}{4}N_{se}\cos(\pi x/\tau). \end{cases} \quad (7)$$

The secondary winding functions, including both the fundamental and end-effect parts, are abstract but can be obtained from the electromagnetic relationship between the primary and

the secondary [4]–[6]. The secondary fundamental winding function $\dot{N}_{rs}$ is derived by

$$\dot{B}_{rs} = \frac{\mu_0}{g_e}\dot{N}_{rs}\dot{I}_{rs} \tag{8}$$

where $\dot{B}_{rs}$ and $\dot{I}_{rs}$ are the secondary fundamental complex flux density and secondary fundamental complex current, respectively. Based on the air-gap flux density steady equation, $\dot{B}_{rs}$ can be expressed by

$$\dot{B}_{rs} = \frac{(3\mu_0/4g_e)N_{se}}{\sqrt{1+(1/sG)^2}} I_s \exp\left[j(\omega_e t - \pi x/\tau + \theta_s)\right] \tag{9}$$

where s is the slip, G is the goodness factor, $\theta_{\rm s}$ is the angle between the primary and secondary fundamental currents, $I_{\rm s}$ is the root-mean-square (RMS) value of the primary phase current, and $\omega_{\rm e}$ is the angular frequency of the power supply. According to the 1-D model of the LIM depicted in Fig. 3 [3], the secondary leakage inductance can be neglected for its smaller value. Hence, the relationship between the primary and the secondary current is described as

$$\dot{I}_{rs} = \dot{I}_s \frac{-jX_m}{jX_m + \frac{R_r}{s}} = \frac{-I_s}{\sqrt{1+(1/sG)^2}} \exp\left[j(\omega_e t + \theta_s)\right] \tag{10}$$

where $X_{\rm m}$ and $R_{\rm r}$ are the mutual inductance reactance and secondary resistance. Hence, based on (8)–(10), the secondary fundamental winding functions $\dot{N}_{rs}$ are indicated by

$$\begin{cases} N_{\alpha rs}(x) = \frac{3}{4}N_{se}\sin(\pi x/\tau) \\ N_{\beta rs}(x) = -\frac{3}{4}N_{se}\cos(\pi x/\tau). \end{cases} \tag{11}$$

Similar to the solution of the secondary fundamental part, the secondary end-effect part winding function $\dot{N}_{re}$ can be deduced by

$$\dot{B}_{re} = \frac{\mu_0}{g_e}\dot{N}_{re}\dot{I}_{re} \tag{12}$$

where $\dot{B}_{re}$ and $\dot{I}_{re}$ are the secondary end-effect complex flux density and current, respectively. Based on the air-gap flux density dynamic equation, $\dot{B}_{re}$ can be derived by [10], [19]

$$\dot{B}_{re} = \frac{\frac{3\mu_0}{4g_e}N_{se}I_s\left(\frac{1}{\alpha_2} + sG\frac{\pi}{\tau} + j\frac{\pi}{\tau_e}\right)}{\left(\frac{1}{\alpha_1}+\frac{1}{\alpha_2}+j\frac{2\pi}{\tau_e}\right)(1+jsG)} \times \exp(-x/\alpha_1)\exp\left[j\left(\omega_e t - \frac{\pi x}{\tau_e}\right)\right]. \tag{13}$$

There are three kinds of flux density waves in air gap, normal flux density wave, entry-end-effect flux density wave, and exit-end-effect flux density wave. α_1 is the length of the entry-end-effect wave penetration coefficient, α_2 is the length of the exit-end- effect wave penetration coefficient, and $\tau_{\rm e}$ is the half-wave length of the end-effect wave. These three parameters can bring some influence on traveling distances of entry- and exit-end-effect flux density waves in the air gap [19]. With regard to the normal traveling flux density, it is similar to the RIM, whose pitch is 2τ period, whereas the entry- and exit-end-effect waves are brought by the end effect from the primary cut-open magnetic paths (both entry and exit terminals), whose pitch are $2\tau_e$ period. Take the SLIM in the linear metro for example. α_1 is 0.4 m, and α_2 is 2 mm at a base speed of 40km/h; hence, the exit-end-effect wave more quickly attenuates than the entrance-end-effect wave. In general, τ (almost 0.25 m) is constant in different speed levels, whereas $\tau_{\rm e}$ (about 0.1 m at the base speed) is variable in different speed levels, which can quickly increase as the speed goes up [24].

Based on [3] and [8], $\dot{I}_{re}$ is

$$\dot{I}_{re} = K\frac{1}{1+jsG}I_s\exp(j\omega_e t) \tag{14}$$

where K is a function of the SLIM operation velocity, primary length, and slip frequency. Based on (12)–(14), the secondary end-effect winding function $\dot{N}_{re}$ is expressed as

$$\begin{cases} N_{\alpha re}(x) = -\frac{N_2}{K}\exp(-x/\alpha_2)\sin(\pi x/\tau_e - \theta_e) \\ N_{\beta re}(x) = \frac{N_2}{K}\exp(-x/\alpha_2)\cos(\pi x/\tau_e - \theta_e) \end{cases} \tag{15}$$

where N_2 and $\theta_{\rm e}$ are related to the slip, goodness factor, and SLIM structural parameters, and they can be described as

$$N_2 = \frac{\frac{-3N_{se}}{4}\sqrt{\left(\frac{1}{\alpha_2}+sG\frac{\pi}{\tau}\right)^2+\left(\frac{\pi}{\tau_e}\right)^2}}{\sqrt{\left(\frac{1}{\alpha_1}+\frac{1}{\alpha_2}\right)^2+\left(\frac{\pi}{\tau_e}\right)^2}}$$

$$\theta_e = \tan^{-1}\frac{\frac{\pi}{\tau_e}}{\frac{1}{\alpha_2}+sG\frac{\pi}{\tau}} - \tan^{-1}\frac{\frac{\pi}{\tau_e}}{\frac{1}{\alpha_1}+\frac{1}{\alpha_2}}.$$

According to aforementioned three groups of winding function equations, it is interesting to see that the primary two-axis parts are the same as the secondary fundamental parts, which are sinusoidal waves within the primary length. Because of the influence of the primary half-filled slots, the β-axis wave can be regarded as lagging the α-axis by approximately $\pi/2$ [9]. The secondary end-effect parts gradually attenuate from the entrance side to the exit side due to the influence of the longitudinal end effect [25].

According to the fundamental theory of electrical machinery, the SLIM voltage equation is given in matrix form by

$$\vec{u} = [R]\vec{i} + \frac{d\vec{\lambda}}{dt} + v_2\frac{\pi}{\tau}[U]\vec{\lambda} \tag{16}$$

where several vectors are expressed as follows:

$$\bar{\lambda} = [L]\vec{i}, \quad \vec{u} = [u_{\alpha s}, u_{\beta s}, 0, 0]^T, \quad \vec{i} = [i_{\alpha s}, i_{\beta s}, i_{\alpha r}, i_{\beta r}]^T$$

$$[R] = \begin{bmatrix} R_s & 0 & 0 & 0 \\ 0 & R_s & 0 & 0 \\ 0 & 0 & R_r & 0 \\ 0 & 0 & 0 & R_r \end{bmatrix}, \quad [U] = \begin{bmatrix} 0 & 0 & 0 & 0 \\ 0 & 0 & 0 & 0 \\ 0 & 0 & 0 & 1 \\ 0 & 0 & -1 & 0 \end{bmatrix}$$

where L is an inductance matrix in which the element between any two winding functions mentioned in (7), (11), and (15) may

be calculated by

$$L_{12} = \frac{2\mu_0 l_\delta}{3g_e} \int_0^{p\tau} N_1(x) N_2(x) dx \tag{17}$$

where $N_1(\mathrm{x})$ and $N_2(\mathrm{x})$ are two arbitrary winding functions, l_δ is the primary stack width, and p is the number of primary poles. There are 36 inductances to be calculated, and 18 of these inductances are independent of each other. Different from the RIM, the mutual inductance between the α- and the β-axes such as $L_{\alpha s \beta s}$ is not zero, because its coupling results from half-filled slots. The relationship between the flux linkage and current in the two axes is (18), shown at the bottom of the page, where L_{ls} and L_{lr} are the primary and secondary leakage inductance, respectively. Because of the influence of both half-filled slots and longitudinal end effect, the flux linkage in the α- or β-axis can be affected by the following four current components in the α- and β-axes:

- $i_{\alpha s}$;
- $i_{\beta s}$;
- $i_{\alpha r}$;
- $i_{\beta r}$.

Inserting (18) into (16) and then making further simplification, two groups of voltage equations can be obtained as follows. The voltage equations of the primary winding are

$$\begin{cases} u_{\alpha s} = R_s i_{\alpha s} + L_{ls} p i_{\alpha s} + L_m p(i_{\alpha s} + i_{\alpha r}) + e_{\alpha t} - e_{\alpha s t} \\ u_{\beta s} = R_s i_{\beta s} + L_{ls} p i_{\beta s} + L_m p(i_{\beta s} + i_{\beta r}) + e_{\beta t} - e_{\beta s t}. \end{cases} \tag{19}$$

The voltage equations of the secondary fundamental winding are

$$\begin{cases} 0 = e_{\alpha t} + L_m p(i_{\alpha s} + i_{\alpha r}) + L_{lr} p i_{\alpha r} + i_{\alpha r} R_r + e_{\alpha r} \\ 0 = e_{\beta t} + L_m p(i_{\beta s} + i_{\beta r}) + L_{lr} p i_{\beta r} + i_{\beta r} R_r + e_{\beta r} \end{cases} \tag{20}$$

where, in (19) and (20), $e_{\alpha t}$, $e_{\beta t}$, $e_{\alpha s t}$, and $e_{\beta s t}$ are induced voltages, considering the influence by the longitudinal end effects, and $e_{\alpha r}$ and $e_{\beta r}$ are secondary moving voltages, which are calculated by

$$\begin{cases} e_{\alpha t} = p\left[L'_{\alpha \mathrm{s} \alpha r e} i_{\alpha r e} + L'_{\alpha \mathrm{s} \beta r e} i_{\beta r e}\right]; \\ e_{\beta t} = p\left[L_{\beta \mathrm{s} \alpha r e} i'_{\alpha r e} + L_{\beta \mathrm{s} \beta r e} i'_{\beta r e}\right] \\ e_{\alpha s t} = -p L_{\alpha s \beta \mathrm{s}} i_{\beta \mathrm{s}}; \quad e_{\beta s t} = -p L_{\alpha s \beta \mathrm{s}} i_{\alpha \mathrm{s}} \\ e_{\alpha r} = v_2(\pi/\tau)\lambda_{\beta r}; \quad e_{\beta r} = -v_2(\pi/\tau)\lambda_{\alpha r} \end{cases} \tag{21}$$

where p is the differential operator that is equal to d/dt. According to (19)–(21), the equivalent two-axis circuits are illustrated in Fig. 4. From (18). By neglecting the influence of both half-filled slots and longitudinal end effect, these mutual inductances between the α- and β-axes will become zero for the

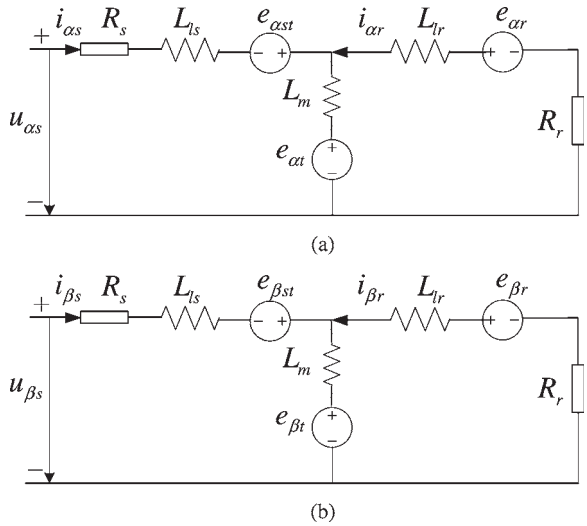

Fig. 4. $\alpha\beta$-axis equivalent circuits of the actual SLIM with half-filled slots and longitudinal end effect. (a) α-axis circuit. (b) β-axis circuit.

noncoupling relationship. Hence, the expression of flux linkage can be simplified as

$$\begin{bmatrix} \lambda_{\alpha s} \\ \lambda_{\beta s} \\ \lambda_{\alpha r} \\ \lambda_{\beta r} \end{bmatrix} = \begin{bmatrix} L_{ls}+L_m & 0 & L_m & 0 \\ 0 & L_{ls}+L_m & 0 & L_m \\ L_m & 0 & L_{lr}+L_m & 0 \\ 0 & L_m & 0 & L_{lr}+L_m \end{bmatrix} \begin{bmatrix} i_{\alpha s} \\ i_{\beta s} \\ i_{\alpha r} \\ i_{\beta r} \end{bmatrix}. \tag{22}$$

Furthermore, the inducted and moving voltages $e_{\alpha t}$, $e_{\beta t}$, $e_{\alpha s t}$, $e_{\beta s t}$, $e_{\alpha r}$, and $e_{\beta r}$ can be rewritten as

$$\begin{cases} e_{\alpha t} = 0; \quad e_{\beta t} = 0 \\ e_{\alpha s t} = 0; \quad e_{\beta s t} = 0 \\ e_{\alpha r} = \omega_r \lambda_{\beta r}; \quad e_{\beta r} = -\omega_r \lambda_{\alpha r} \end{cases} \tag{23}$$

where ω_{r} is the secondary electrical angular speed. The simplified equivalent circuits are indicated in Fig. 5. When the longitudinal end effect and half-filled slots are ignored, i.e., the SLIM totally appears as the RIM, the equivalent circuits in Fig. 5 are similar to the traditional RIM. Different from the RIM, the special traits of the SLIM are the calculation of mutual and end-effect inductances that are functions of the slip, primary excitation frequency, and structure parameters. Moreover, the equivalent circuits in Fig. 5 can be extended to dynamic coordinate references, and the derivation process and final equivalent circuits are similar to the RIM.

According to the energy conversion balance theorem between the primary and the secondary, the thrust is described as

$$F_e = (3\pi/2\tau)[i_1]^T [G_{sv}][i_1] \tag{24}$$

$$\begin{bmatrix} \lambda_{\alpha s} \\ \lambda_{\beta s} \\ \lambda_{\alpha r} \\ \lambda_{\beta r} \end{bmatrix} = \begin{bmatrix} L_{ls}+L_m+L'_{\alpha s \alpha r e} & L_{\alpha s \beta s}+L'_{\alpha s \beta r e} & L_m+L'_{\alpha s \alpha r e} & L_{\alpha s \beta r}+L'_{\alpha s \beta r e} \\ L_{\alpha s \beta s}+L'_{\beta s \alpha r e} & L_{ls}+L_m+L'_{\beta s \beta r e} & L_{\beta s \alpha r}+L'_{\beta s \alpha r e} & L_m+L'_{\beta s \beta r e} \\ L_m+L'_{\alpha r \alpha r e} & L_{\alpha r \beta s}+L'_{\alpha r \beta r e} & L_{lr}+L_m+L'_{\alpha r \alpha r e} & L_{\alpha r \beta r}+L'_{\alpha r \beta r e} \\ L_{\beta r \alpha s}+L'_{\beta r \alpha r e} & L_m+L'_{\beta r \beta r e} & L_{\beta r \alpha r}+L'_{\beta r \alpha r e} & L_{lr}+L_m+L'_{\beta r \beta r e} \end{bmatrix} \begin{bmatrix} i_{\alpha s} \\ i_{\beta s} \\ i_{\alpha r} \\ i_{\beta r} \end{bmatrix} \tag{18}$$

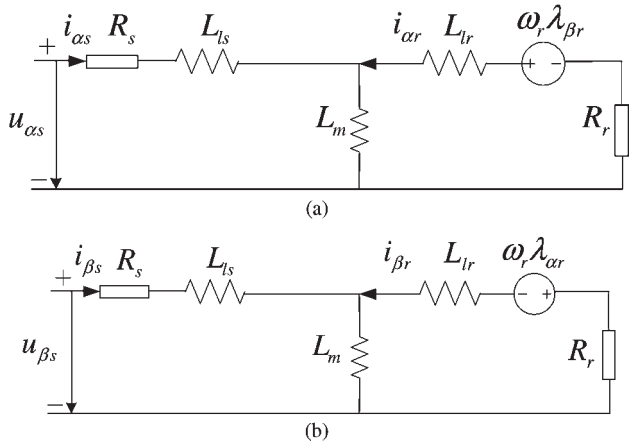

Fig. 5. $\alpha\beta$-axis equivalent circuits of the ideal SLIM without the influences of half-filled slots and longitudinal end effect. (a) α-axis circuit. (b) β-axis circuit.

where the matrix i_1, including the end-effect part, is expressed by

$$[i_1] = [i_{\alpha s}, i_{\beta s}, i_{\alpha r}, i_{\beta r}, (i_{\alpha s} + i_{\alpha r}), (i_{\beta s} + i_{\beta r})]^T \quad (25)$$

and matrix G_{sv} is the speed voltage coefficient matrix, which may be calculated similar to the inductance matrix L.

The input active power is

$$p_{in} = \frac{3}{2}(u_{\alpha s} i_{\alpha s} + u_{\beta s} i_{\beta s}). \quad (26)$$

The input reactive power is

$$q_{in} = \frac{3}{2}(u_{\beta s} i_{\alpha s} - u_{\alpha s} i_{\beta s}). \quad (27)$$

The output active power is

$$p_{out} = (F_e - F_m) v_2 \quad (28)$$

where $F_{\rm m}$ is the total mechanical resistant force that involves wind and friction forces.

The power factor is

$$\cos\varphi = p_{in} / \sqrt{p_{in}^2 + q_{in}^2}. \quad (29)$$

The efficiency is

$$\eta = p_{out} / p_{in}. \quad (30)$$

III. Simulation and Experiments

The aforementioned derivations describe the dynamic state of the SLIM in differential linkage equations. The equations can numerically be solved step by step by executing in the MATLAB/Simulink environment. In most dynamic cases, the state variables include the secondary linkages and primary currents. The equations can also readily be used in the steady-state analysis by simply setting d/dt to $\mathrm{j}\omega_{\rm e}$ in (16). The following two motors are analyzed in this paper, as illustrated in Figs. 6 and 7, respectively: 1) an arc induction motor (motor A) and 2) one SLIM applied in a linear metro train (motor B) [2], [17]. Their main dimensions and electrical parameters are

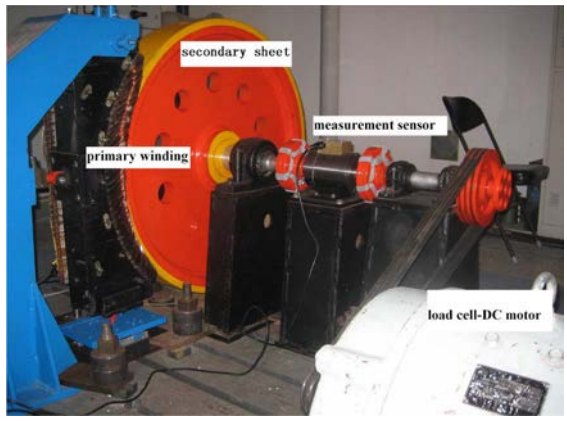

Fig. 6. Prototype of the arc induction motor (motor A).

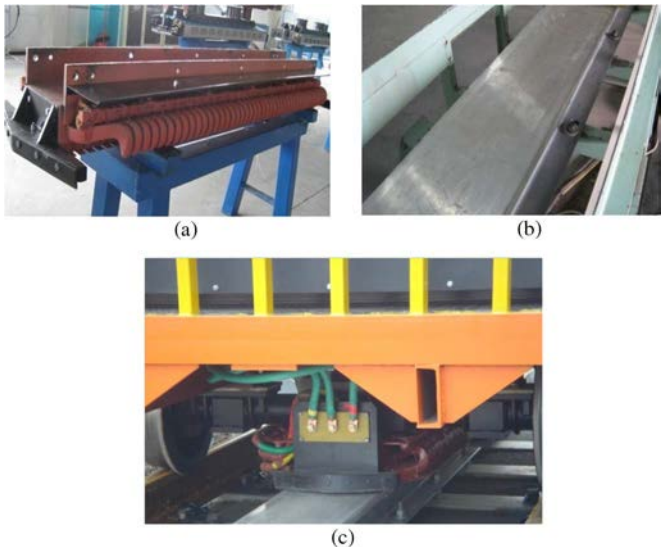

Fig. 7. Arrangement of the SLIM and application on the train (motor B). (a) Primary. (b) Secondary. (c) Vehicle.

shown in Table I. The experimental method for deriving the five SLIM electrical parameters can be referred in [21]. Generally speaking, it is similar to the RIM in the following three steps:

Step 1) Direct-current (dc) phase resistance $R_{\rm dc}$. An exact value of the primary dc phase resistance $R_{\rm dc}$ can be obtained by measuring the dc voltage between winding terminals and the dc that corresponds to the rated alternating current (ac).

Step 2) Testing of open secondary circuit (decision on $R_{\rm s}$, $L_{\rm m}$, and $L_{\rm ls}$). The actual (ac excitation) the primary phase winding resistance $R_{\rm s}$, mutual inductance $L_{\rm m}$, and primary leakage inductance $L_{\rm ls}$ can be obtained by disconnecting the secondary branch of the equivalent circuit.

Step 3) Testing of blocked secondary circuit (decision on $R_{\rm r}$ and $L_{\rm lr}$). By performing the blocked secondary test with the real reaction rail, the secondary resistance $R_{\rm r}$ and leakage inductance $L_{\rm lr}$ can be obtained.

The testing analysis is combined with investigation by the numerical circuit method and finite-element algorithm. Some unreasonable data should be neglected.

TABLE I
MAIN DIMENSIONS AND PARAMETERS OF THE TWO MOTORS

Items		Motor A	Motor B
Primary	Pole pitch/m	0.117	0.2808
	Pole pairs	3	4
	Length/m	0.798	2.476
	Width/m	0.1	0.3
	Rated frequency/Hz	50	25
	Number of slots	41	79
	Number of stator series turns per phase	216	192
	Number of slots per pole per phase	2	3
	Number of half-filled primary end slots	5	7
	Iron depth/m	0.099	0.128
	Number of coil pitch/slot	5	7
	Number of conductor per slot	36	16
Air gap length/m		0.010	0.009
Secondary	Width/m	0.16	0.36
	Sheet thickness/m	0.005	0.007
	Back iron depth/m	0.021	0.025
Electrical parameters	Stator resistance /Ω	0.4253	0.0226
	Stator leakage inductance /H	2.14E-3	1.03 E-3
	Mutual inductance /H	11.51 E-3	5.58 E-3
	Rotor resistance/Ω	0.221	0.127
	Rotor leakage inductance /H	0.55 E-3	0.17E-3

As shown in Fig. 6, the arc induction machine prototype experimental bench has a rotor that is formed on the rim of the large-radius flywheel, whose primary is fed by a converter. The load cell is a dc machine that is connected to the shaft of the SLIM rig by belts. The dc machine can operate at any desired speed and load below the rating values to provide different working points. The measurement sensors located between the SLIM and the dc load can record the SLIM velocity, load power, and thrust.

Fig. 7 shows the structure of the primary, the secondary, and the whole SLIM in the train. The primary is placed in the bogie under the vehicle body, and the secondary sheet is flattened in the experimental linear metro line.

A. Steady-State Simulation and Testing

Fig. 8 presents different thrust curves of two motors under constant-current–constant-frequency excitation. As shown in this figure, the maximal thrust of the SLIM, different from the RIM, will gradually decrease as the speed goes up by the influence of longitudinal end effects, particularly in the area of high speed, whereas the RIM has constant maximal thrust in different frequencies for constant flux linkage in the air gap by its symmetry structure.

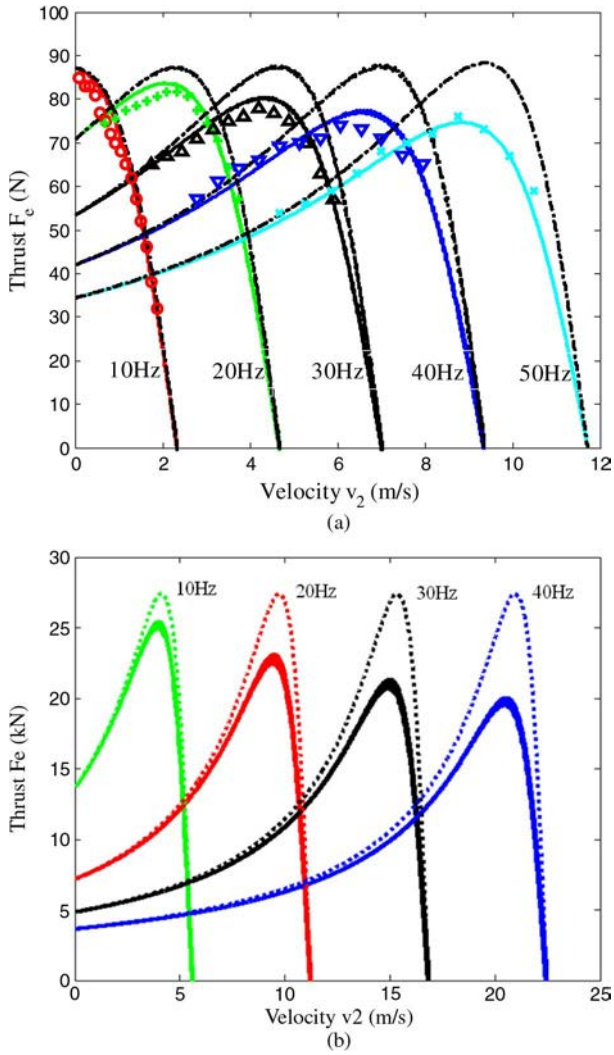

Fig. 8. Steady-state thrust curves with constant current and variable frequency. (a) Motor A under 11 A (real lines are the thrusts without end effects, dashed lines the thrusts with end effects, and other shape lines are the measured). (b) Motor B under 280 A (real lines are the thrusts without end effect and dashed lines the thrusts with end effects. All results are in simulation).

Fig. 9 shows the thrust excited by constant voltage in different frequencies by the steady-state equations. In Fig. 9(a), it starts up under 220-V constant primary line voltage, and its current is a little larger than the rating value for its smaller equivalent reactance. As the speed increases, the torque more quickly decreases than by the constant current in Fig. 8(a) for its quicker air-gap flux attenuation. In general, the thrust prediction reasonably agrees with the measurement in various velocities. In Fig. 9(b), it is excited by the primary line voltage 530 V. The general trend of thrust is similar to Fig. 9(a).

The thrust of the SLIM applied in transportation is one of the most important indices. The actual SLIM control scheme often includes the following two regions: 1) the “constant-current” region and 2) the “constant-power” region. Below the base speed, the primary phase current and slip frequency are kept constant. Because of the power conditioner voltage limitation, the constant-voltage operation is encountered above the base speed. The phase current very quickly decreases due to the increasing total impedance. To meet the drive system requirement, it is necessary to linearly increase the slip frequency to

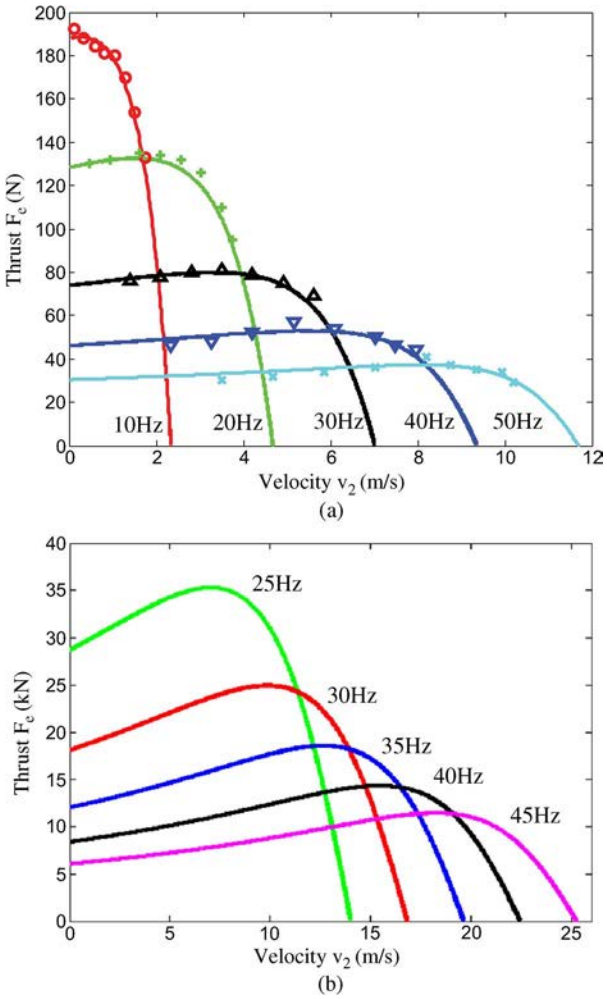

Fig. 9. Steady-state thrust curves with constant voltage and variable frequency. (a) Motor A under 220-V line voltage (real lines are the thrusts with end effects, and other shape lines are the measured). (b) Motor B under 530-V line voltage (all results are the thrusts with end effect in simulation).

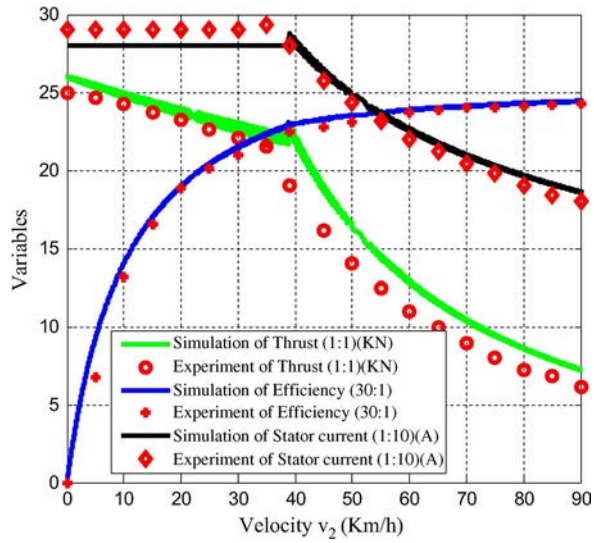

Fig. 10. Simulated and measured performance curves in the whole operation range.

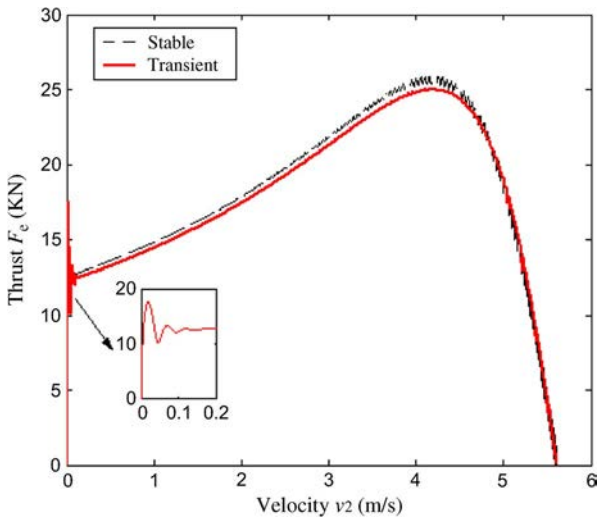

Fig. 11. Thrust curves with constant current and frequency calculated at the steady and dynamic states.

prevent quick thrust reduction. Here, the steady-state drive performance of motor B in the overall working region is analyzed and compared with measurements, including the phase current, thrust, and efficiency curves, as shown in Fig. 10. The base speed is 40 km/h. Simulation on the phase current, thrust, and efficiency is made according to the steady equations of the equivalent models. As shown in the figure, the simulated phase current is close to the measurements. It is kept constant below the base speed and linearly decreases beyond the base speed. The thrust below the base speed decreases a little as the speed goes up due to the end effect, although the phase current is constant. Beyond the base point, the thrust linearly decreases due to the reducing phase current. The error in the base speed is obvious, because the control manner and slip frequency have been changed, but the efficiency calculation and measurement reasonably agree with each other.

B. Dynamic-State Simulation and Testing

Fig. 11 shows the thrust curves of motor B calculated by the steady- and dynamic-state equations. In the entire range, the primary current is controlled to be constant at 280 A, and the primary frequency is supposed a constant at 10 Hz. It is apparent that the steady-state thrust is very close to the dynamic-state thrust in addition to the short starting-up procedure due to the electromagnetic transition in the secondary. By the verification of the steady-state model in Section III-A, it is shown that the dynamic model is also reasonable to make performance prediction. As shown in Fig. 11, it is interesting that there are double-frequency (20-Hz) thrust ripples as the SLIM starts up. This case is due to the electromagnetic dynamics in the secondary circuits produced by the longitudinal end effects.

Fig. 12 shows the constant-current start-up process, including the velocity, thrust, secondary fundamental, and eddy-current curves. In the overall operation region, the motor has a constant stator current of 280 A and a constant primary frequency of 25 Hz. As shown in the figure, the secondary fundamental current, similar to the RIM, gradually decreases as the speed rises and is almost zero close to the synchronous point. However, the secondary end-effect part ascends with incremental speed,

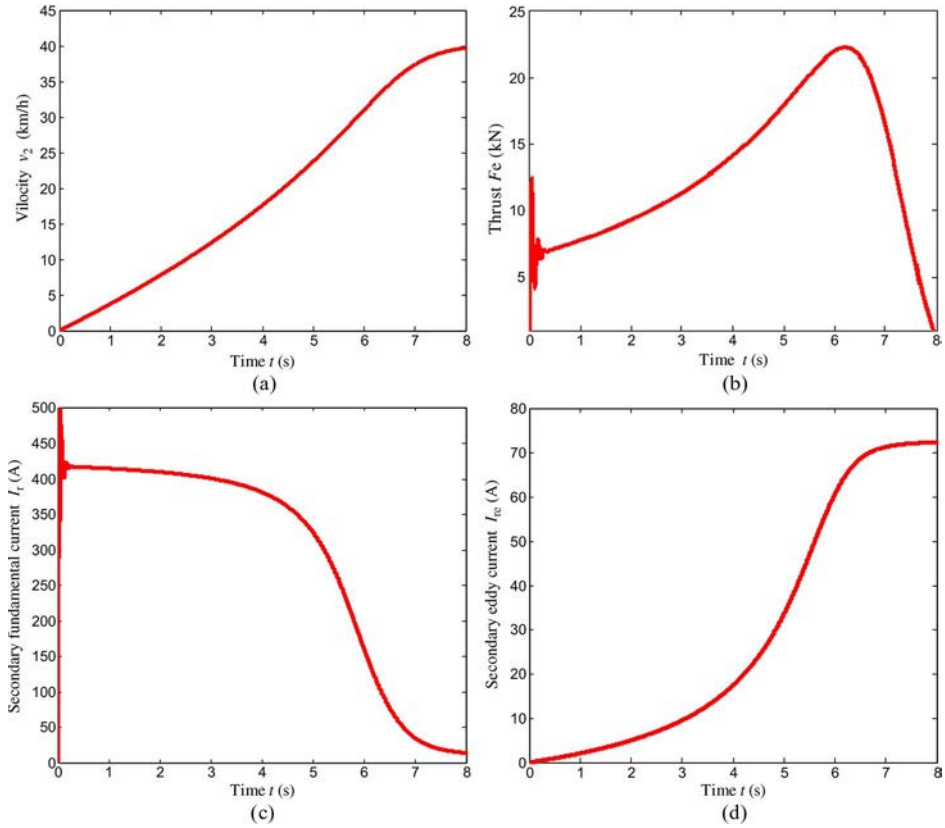

Fig. 12. Constant-current start-up performance analysis. (a) Velocity. (b) Thrust. (c) Secondary fundamental current (RMS). (d) Secondary eddy current (RMS).

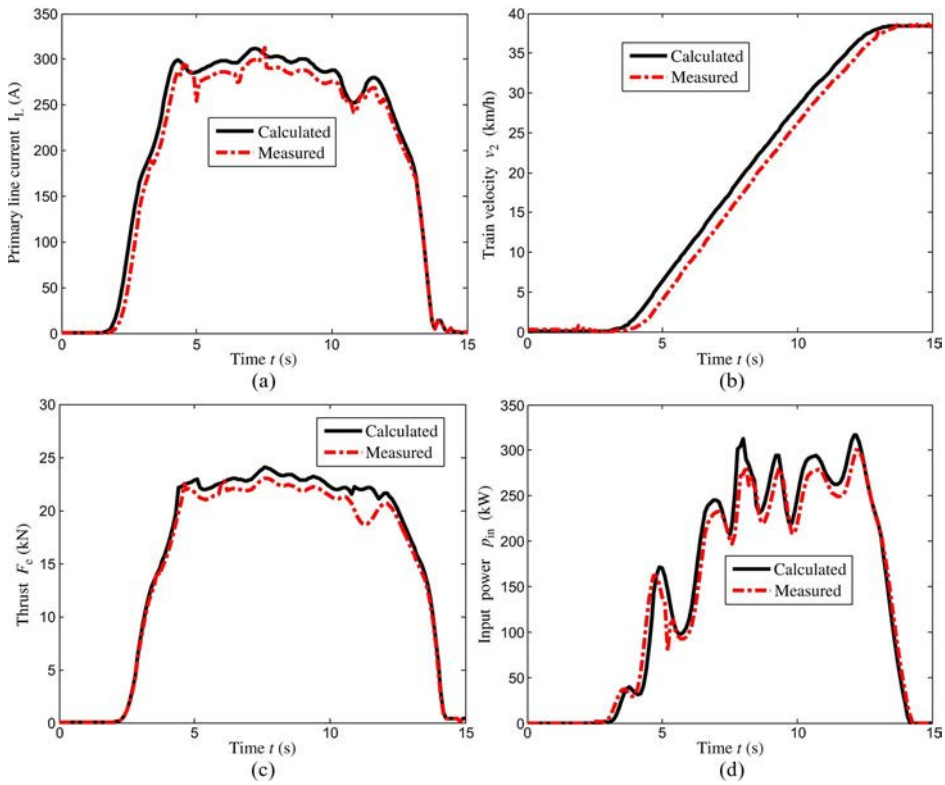

Fig. 13. Variable-frequency–variable-voltage start-up performance analysis of motor B. (a) Stator current. (b) Velocity. (c) Thrust. (d) Input power.

reaching a maximum close to the synchronous speed, because the quick air-gap flux linkage change results from the longitudinal end effect.

Fig. 13 shows the variable-frequency–variable-voltage start-up process of motor B. The primary frequency proportionally varies from 2 Hz to 25 Hz with increasing primary voltage to

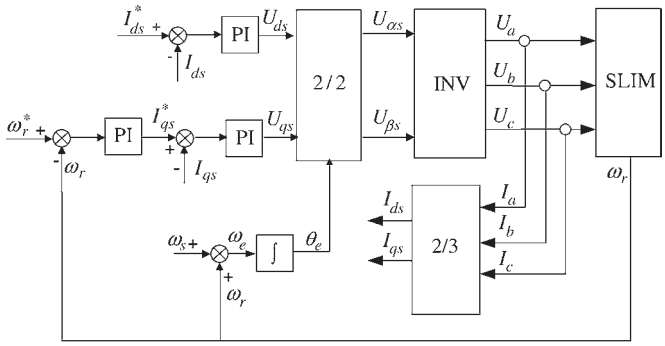

Fig. 14. Simple diagram of the indirect-rotor field-orientation control algorithm.

keep a comparatively constant air-gap flux linkage. The test is carried out on the experimental linear metro line in cooperation with a company, as illustrated in Fig. 7(c). During this testing, the primary two-phase voltages, two-phase currents, and operating speed are sampled by corresponding sensors and input into a Yokogawa DL750 oscillometric recorder. The sampling frequency for voltage is about 20 kHz, and measured voltage data can directly be input into the dynamic equations for step-by-step simulation. Some typical criteria by predication are compared with their measurements, including the stator phase current, train velocity, thrust, and input power. It is shown that the calculation agrees with the measurements in general.

To further verify the new model, the traditional indirect rotor field control algorithm was executed on the arc induction motor (motor A). The flowchart of the control scheme is illustrated in Fig. 14, which includes the following three closed loops: 1) rotor speed loop; 2) d-axis current loop; and 3) q-axis current loop. These loops are modified by three proportional–integral (PI) regulators, which are similar to the RIM.

Fig. 15 shows the theoretical and measured curves of velocity v_2 and thrust $F_{\rm e}$. The velocity is given by 6.28 m/s, and the field current is kept at a constant of 8 A in the whole process. The SLIM is accelerated from 0 m/s to 6.28 m/s in the first 40 s, then operated with constant velocity for 20 s, and finally decelerated in almost 20 s. Although excited by constant current $I_{\rm ds}$, the thrust is attenuated a little for its longitudinal end effects. Considering different friction and windage resistances between theoretical simulation and practical experiment, the performance curves in Fig. 15(a) reasonably validate the performance curves in Fig. 15(b).

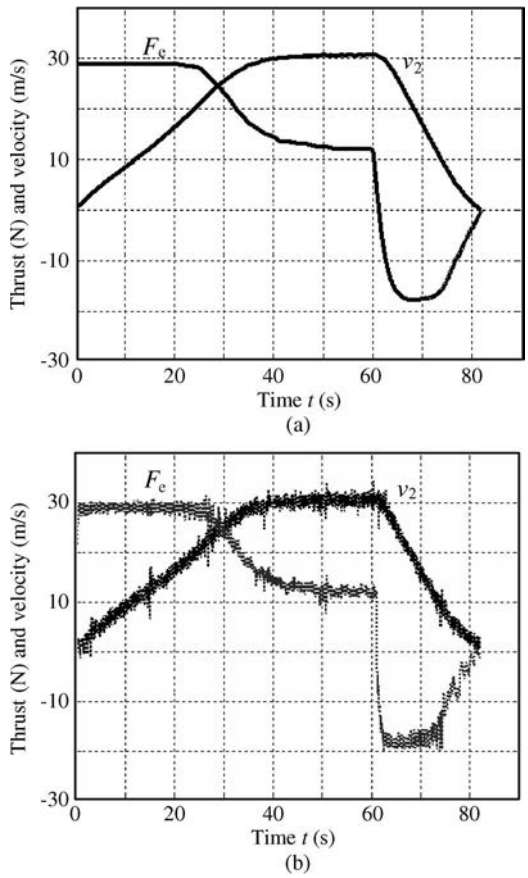

Fig. 15. Thrust and velocity curves (the ratio of thrust to velocity is 1 : 3 or 5 : 1). (a) Calculated. (b) Measured.

IV. Conclusion

One new equivalent model of the SLIM has been presented from the winding distribution described by the winding function method. The SLIM is first supposed to have the following three groups of winding functions: 1) primary; 2) secondary fundamental; and 3) secondary end effect. The primary stationary two-axis winding functions are derived from the stationary three-phase winding distributions joined by 3/2 static-axis transformation. The secondary fundamental and end-effect winding functions are obtained based on the electromagnetic distribution relationship between the primary and the secondary. According to the three groups of windings, the influence of the longitudinal end effect and half-filled slots can automatically be described by the corresponding end-effect mutual inductance and half-filled slot inductance. Moreover, the equivalent voltage and linkage equations are derived using the theory of the RIM to construct the equivalent circuits, which can analyze both the steady- and dynamic-state performance similar to the RIM. By comprehensive simulation and/or experiments on different working states, the proposed circuits can be regarded as a useful tool for investigating different SLIM dynamic- and steady-state performance. It is an effective model for the electromagnetic design and performance prediction for the SLIM particularly applied in the linear metro.

Acknowledgment

The authors would like to thank Prof. Y. Li and Associate Prof. J. Ren of the Institute of Electrical Engineering, Chinese Academy of Sciences, Beijing, China, for their active suggestions.

References

[1] X. L. Long, *Theory and Magnetic Design Method of Linear Induction Motor*. Beijing, China: Science, 2006.
[2] W. Xu, J. Zhu, Y. Zhang, Y. Li, Y. Wang, and Y. Guo, "An improved equivalent circuit model of a single-sided linear induction motor," *IEEE Trans. Veh. Technol.*, vol. 59, no. 5, pp. 2277–2289, Jun. 2010.
[3] M. Poloujadoff, *The Theory of Linear Induction Machinery*. Oxford, U.K.: Clarendon, 1980.
[4] G. Kang and K. Nam, "Field-oriented control scheme for linear induction motor with the end effect," *Proc. Inst. Elect. Eng.—Elect. Power Appl.*, vol. 152, no. 6, pp. 1565–1572, Nov. 2005.

[5] J. Duncan, "Linear induction motor equivalent circuit model," *Proc. Inst. Elect. Eng. B—Elect. Power Appl.*, vol. 130, no. 1, pp. 51–57, Jan. 1983.
[6] J. H. Sung and N. Kwanghee, "A new approach to vector control for a linear induction motor considering end effects," in *Conf. Rec. IEEE IAS Annu. Meeting*, 1999, pp. 2284–2289.
[7] T. Higuchi and S. Nonaka, "On the design of high-efficiency linear induction motors for linear metro," *Elect. Eng. Jpn.*, vol. 137, no. 2, pp. 36–43, Nov. 2001.
[8] J. H. Park and Y. S. Baek, "Design and analysis of a maglev planar transportation vehicle," *IEEE Trans. Magn.*, vol. 44, no. 7, pp. 1830–1836, Jul. 2008.
[9] T. A. Lipo and T. A. Nondahl, "Pole-by-pole d–q model of a linear induction machine," *IEEE Trans. Power App. Syst.*, vol. PAS-98, no. 2, pp. 629–642, Mar./Apr. 1979.
[10] W. Xu, "Research on the performance of single-sided linear induction motor," Ph.D. dissertation, Inst. Elect. Eng., Chinese Acad. Sciences, Beijing, China, 2008.
[11] B. J. Lee, D. H. Koo, and Y. H. Cho, "Investigation of linear induction motor according to secondary conductor structure," *IEEE Trans. Magn.*, vol. 45, no. 6, pp. 2839–2842, Jun. 2009.
[12] R. Thornton, "Linear-motor-powered transportation," *Proc. IEEE*, vol. 97, no. 11, pp. 1754–1757, Nov. 2009.
[13] R. Hellinger and P. Mnich, "Linear-motor-powered transportation: History, present status, and future outlook," *Proc. IEEE*, vol. 97, no. 11, pp. 1892–1900, Nov. 2009.
[14] C. A. Lu, "A new coupled-circuit model of a linear induction motor and its application to steady-state, transient, dynamic and control studies," Ph.D. dissertation, Dept. Elect. Eng., Queen Univ., Kingston, ON, Canada, 1993.
[15] R. Haghmaram and A. Shoulaie, "Transient modeling of multiparallel tubular linear induction motors," *IEEE Trans. Magn.*, vol. 42, no. 6, pp. 1687–1693, Jun. 2006.
[16] J. F. Gieras, G. E. Dawson, and A. R. Eastham, "A new longitudinal end effect factor for linear induction motors," *IEEE Trans. Magn.*, vol. EC-2, no. 1, pp. 152–159, Mar. 1987.
[17] W. Xu, J. Zhu, Y. Zhang, Z. Li, Y. Li, Y. Wang, Y. Guo, and Y. J. Li, "Equivalent circuits for single-sided linear induction motors," *IEEE Trans. Ind. Appl.*, vol. 46, no. 6, pp. 2410–2423, Nov./Dec. 2010.
[18] I. E. Davidson and J. F. Gieras, "Performance analysis of a shaded-pole linear induction motor using symmetrical components, field analysis, and finite element method," *IEEE Trans. Energy Convers.*, vol. 15, no. 1, pp. 24–29, Mar. 2000.
[19] S. Yamamura, *Theory of Linear Induction Motors*. Tokyo, Japan: Tokyo Press, 1978.
[20] J. F. Gieras, *Linear Induction Drives*. Oxford, U.K.: Clarendon, 1980.
[21] Y. Mori, S. Torii, and D. Ebihara, "End effect analysis of linear induction motor based on the wavelet transform technique," *IEEE. Trans. Magn.*, vol. 35, no. 5, pp. 3739–3741, Sep. 1999.
[22] D. Hall, J. Kapinshi, M. Krefta, and O. Christianson, "Transient electromechanical modeling for short secondary linear induction machines," *IEEE Trans. Energy Convers.*, vol. 23, no. 3, pp. 789–795, Sep. 2008.
[23] J. H. H. Alwash and S. H. Ikhwan, "Generalized approach to the analysis of asymmetrical three-phase induction motors," *Proc. Inst. Elect. Eng.—Elect. Power Appl.*, vol. 142, no. 2, pp. 87–96, Mar. 1995.
[24] J. H. H. Alwash and J. F. Eastham, "Permeance harmonic analysis of short-stator machines," *Proc. IEE*, vol. 123, no. 12, pp. 1335–1340, Dec. 1976.
[25] G. Kang, J. H. Kim, and K. Nam, "Parameter estimation scheme for low-speed linear induction motors having different leakage inductances," *IEEE Trans. Ind. Electron.*, vol. 50, no. 4, pp. 708–716, Aug. 2003.

Wei Xu (M'09) received the B.E.–B.A. and M.E. degrees in electrical engineering from Tianjin University, Tianjin, China, in 2002 and 2005, respectively, and the Ph.D. degree in electrical engineering from the Chinese Academy of Sciences, Beijing, China, in 2008.

From September 2008 to August 2011, he was a Postdoctoral Fellow with the Center for Electrical Machines and Power Electronics, University of Technology Sydney (UTS), Sydney, NSW, Australia, where his research was supported by a UTS Early Career Researcher Grant and international research Grants. Since September 2011, he has been a Vice Chancellor Research Fellow (Tenure Track) with RMIT University, Melbourne, Vic., Australia. His research interests include electromagnetic design and advanced control algorithms on different kinds of linear/rotary machines.

Guangyong Sun (M'09) received the B.E. and Ph.D. degrees from Hunan University, Changsa, China, in 2003 and 2011, respectively.

He is currently with the State Key Laboratory of Advanced Design and Manufacture for Vehicle Body, Hunan University. His research interests include sheet metal forming, structure optimization, and automotive safety.

Guilin Wen is currently a Full Professor and the Associate Dean with the College of Mechanical and Vehicle Engineering, Hunan University, Changsa, China. His research interests include mechanical structure optimization, nonlinear dynamics, and vibration control for different vehicles.

Zhengwei Wu (M'09) received the B.S. and M.S. degrees from the University of Science and Technology of China, Hefei, China, in 2000 and 2005, respectively, and the Ph.D. degree from the City University of Hong Kong, Kowloon, Hong Kong, in collaboration with the University of Sydney, Sydney, NSW, Australia, in 2010.

He is currently with the Department of Physics and Materials Science, City University of Hong Kong. His research interests include plasma engineering and quantum plasmas.

Paul K. Chu (F'03) received the B.S. degree in mathematics from the Ohio State University, Columbus, in 1977 and the M.S. and PhD degrees in chemistry from Cornell University, Ithaca, NY, in 1979 and 1982, respectively.

He is currently with the Department of Physics and Materials Science, City University of Hong Kong, Kowloon, Hong Kong. His research interests include plasma surface engineering and various types of materials and nanotechnology.